Electronic Supplementary Material (ESI) for Journal of Materials Chemistry A.

From Pollution to Energy Storage: Leveraging Hydrogen Sulfide with SU-101 Cathodes in Lithium-Sulfur Batteries

Raul A. Marquez,*[a] Juan L. Obeso,†[b,c] Rinish Reddy Vaidyula,†[a] Valeria B. López-Cervantes,†[b] Ricardo A. Peralta,[d] Pablo Marín Rosas,[d] José Antonio de los Reyes,[e] C. Buddie Mullins*[a,f,g] and Ilich A. Ibarra*[b,h]

[a] Raul A. Marquez, Rinish Reddy Vaidyula and Prof. C. Buddie Mullins
Department of Chemistry
The University of Texas at Austin
105 E. 24th St. Austin, TX, 78712, USA.

[b] Juan L. Obeso, Valeria B. López-Cervantes and Prof. Ilich A. Ibarra
Laboratorio de Fisicoquímica y Reactividad de Superficies (LaFReS)
Instituto de Investigaciones en Materiales, Universidad Nacional Autónoma de México
Circuito Exterior s/n, CU, Coyoacán, 04510, Ciudad de México, México.
E-mail: argel@unam.mx

[c] Juan L. Obeso
Laboratorio Nacional de Ciencia, Tecnología y Gestión Integrada del Agua (LNAgua)
Instituto Politécnico Nacional, CICATA U. Legaria
Legaria 694 Irrigación, Miguel Hidalgo, CDMX, México.

[d] Pablo Marín Rosas and Prof. Ricardo A. Peralta
Departamento de Química, División de Ciencias Básicas e Ingeniería
Universidad Autónoma Metropolitana-Iztapalapa
Av. San Rafael Atlixco,186, Col. Vicentina, 09340, Ciudad de México, México.

[e] Prof. José Antonio de los Reyes
Laboratory of Environmental Catalysis.
Universidad Autónoma Metropolitana-Iztapalapa
Av. San Rafael Atlixco 186, Col. Vicentina, Ciudad de México, 09340 México.

[f] Prof. C. Buddie Mullins
McKetta Department of Chemical Engineering, The University of Texas at Austin, Austin, Texas 78712, United States.
[g] Prof. C. Buddie Mullins
Texas Materials Institute, The University of Texas at Austin, Austin, Texas 78712, United States.
[h] Prof. Ilich A. Ibarra
On Sabbatical as “Catedra Dr. Douglas Hugh Everett” at Departamento de Química.
Universidad Autónoma Metropolitana-Iztapalapa.
Avenida San Rafael Atlixco 186, Leyes de Reforma 1ra Sección, Iztapalapa, Ciudad de México 09310, México.

[†] These authors contributed equally to this work.

Table of contents

S1. Experimental Methods

H_2S Saturation Experiments

The H_2S saturation system (depicted in **Figure S1**) comprises two main components:

A. *The Gas Generator*: Fe_2S_3 is placed in a two-neck round-bottom flask [1]. One neck is sealed with a rubber stopper through which concentrated HCl is introduced using a glass syringe [2], while the other neck connects to the saturation chamber.

B. *The Saturation Chamber*: This component consists of a round flask [3] connected to both a vacuum line [4] and a pressure gauge [5].

First, approximately 15 mg of the sample in a 1.5 mL glass vial is activated in a sand bath at 100 °C under vacuum for 12 hours. The vial is then transferred to the saturation chamber, and the system is evacuated using the vacuum line. H_2S gas is generated by slowly dripping concentrated HCl onto Fe_2S_3. Then, the SU-101 sample is exposed to H_2S gas continuously for 4 and 12 hours.

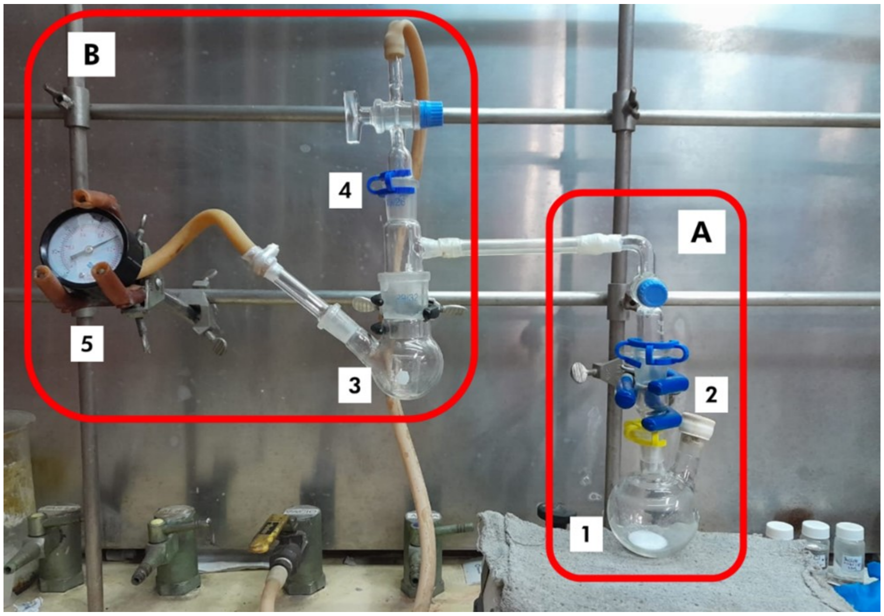

Figure S1. Photograph of the custom setup for *in situ* H_2S saturation experiments.

H_2S Adsorption Measurements

H_2S experiments were conducted using an HP 5890 gas chromatograph with continuous injections of the system exhaust. A single chromatogram was obtained for each injection, and the H_2S signal from each chromatogram was integrated for quantification. Given the known H_2S concentration in the feed, the H_2S concentration was calculated for each injection, assuming that the saturation concentration equals the original feed concentration. Dynamic breakthrough experiments were performed using a homemade system.

SU-101 was activated *in situ* at 120 °C for 2 hours with a constant flow of dry N_2 (25 mL min^{-1}, ultrapure grade 99.98% N_2, Praxair) and then gradually cooled to 25 °C. The H_2S concentration was regulated using a mass flow controller with two lines: dry N_2 and a 15% vol H_2S/N_2 mixture. The gas mixture for the H_2S experiments was set at 10 vol% H_2S with a flow rate of 25 mL min^{-1}. The breakthrough experiments were conducted at 25 °C, and the downstream flow was analyzed using gas chromatography. The sample was reactivated at 25 °C for 15 minutes under a flow of dry N_2 (25 mL min^{-1}).

The H_2S adsorption capacity for each cycle was calculated using **Eq. S1**, where V_{H2S} represents the volumetric capacity of H_2S ($cm^3\ g^{-1}$), m is the adsorbent mass (g), F is the input flow rate ($cm^3\ min^{-1}$), C_f and C_t are the influent and effluent H_2S concentrations, respectively, (vol%), and t is the time (min).

$$V_{H_2S} = \frac{F}{C_f m} \cdot \int_0^t (C_f - C_t) dt \qquad (S1)$$

The adsorption column is equipped with a porous glass bed; therefore, a blank run was conducted before each experiment to account for the column's inherent adsorption contribution. Subsequently, the material-corrected volumetric capacity, $V_{H2S,corr}$, was calculated for each cycle using **Eq. S2**.

$$V_{H_2S,corr} = V_{H_2S,blank} - V_{H_2S,sample} \qquad (S2)$$

The H_2S adsorption capacity is reported as q_{H2S} (mol g^{-1}). This value was approximated using the corrected volumetric adsorption capacity $V_{H2S,corr}$ ($cm^3\ g^{-1}$) and the ideal gas law, expressed as **Eq. S3.** Here, p is the system pressure (77.3 kPa), T is the measurement temperature (298 K), and R is the ideal gas constant (8314.4598 cm^3 kPa K^{-1} mol^{-1}).

$$q_{H_2S} = \frac{V_{H_2S,corr} \cdot p}{R \cdot T} \qquad (S3)$$

S2. Additional Characterization and Results

Characterization of SU-101

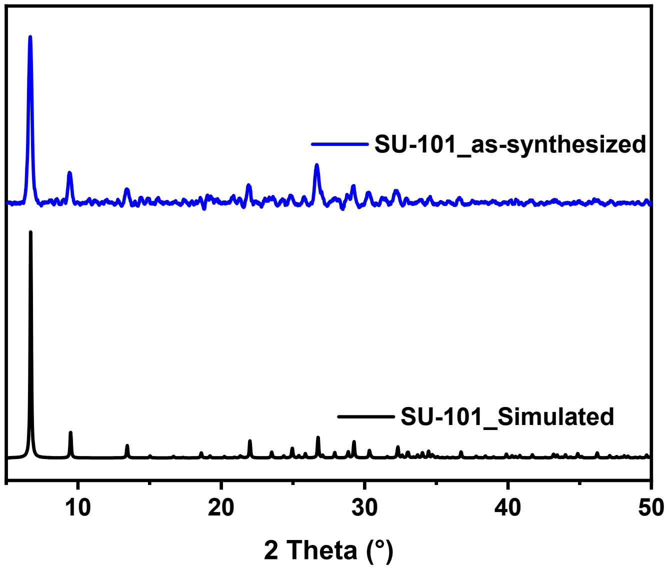

Figure S2. X-ray diffraction pattern of the as-synthesized and simulated SU-101.

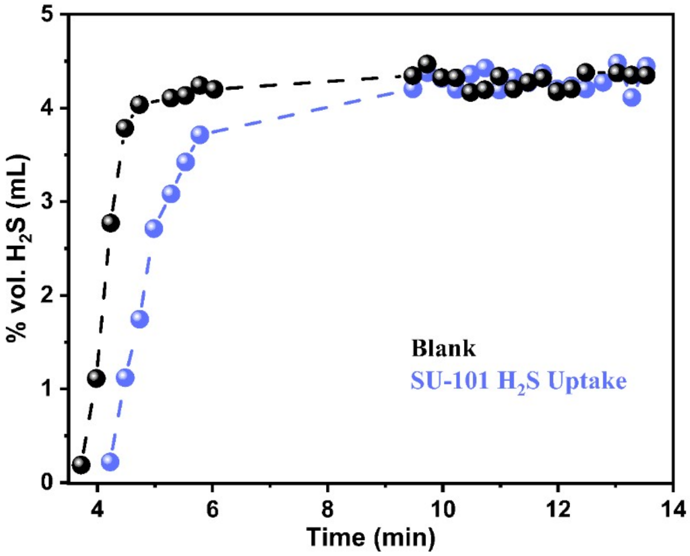

Figure S3. Breakthrough curve of H_2S adsorption using SU-101 at 298 K and 1 bar.

Characterization of SU-101 after exposure to H_2S

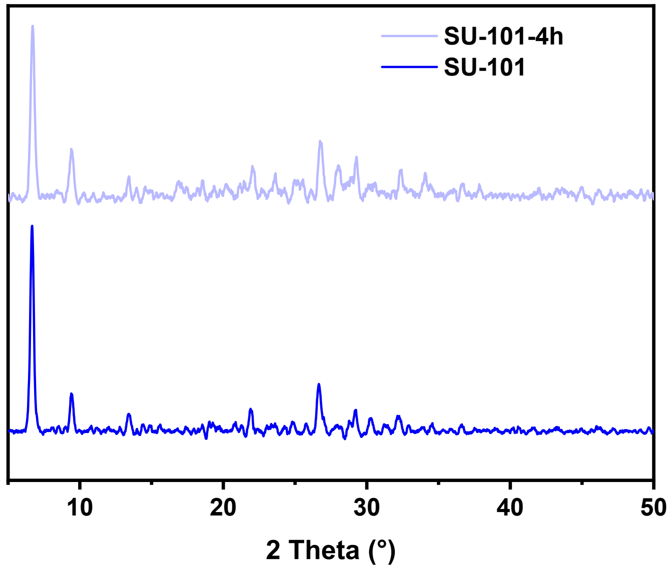

Figure S4. X-ray diffraction pattern of the as-synthesized SU-101 before and after exposure to H_2S gas for 4 hours.

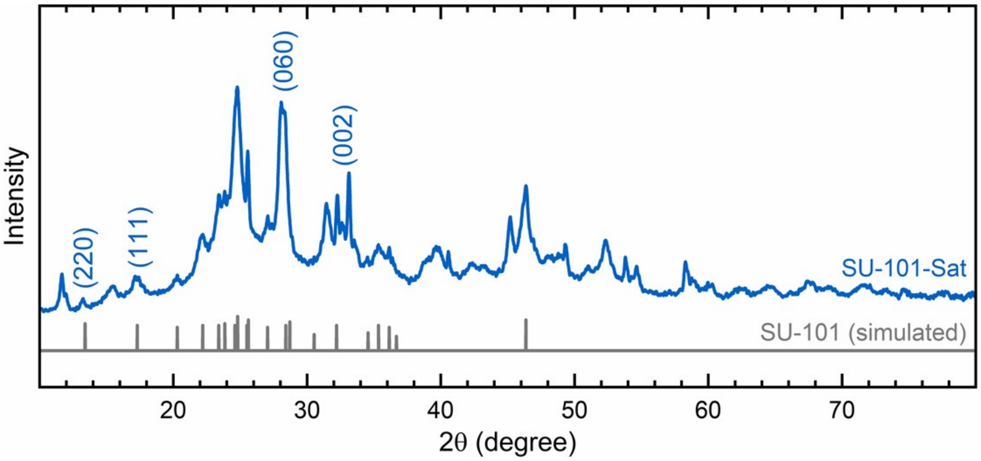

Figure S5. X-ray diffraction pattern of the SU-101-Sat sample. The simulated pattern of the SU-101 MOF is obtained from Ref. 1.

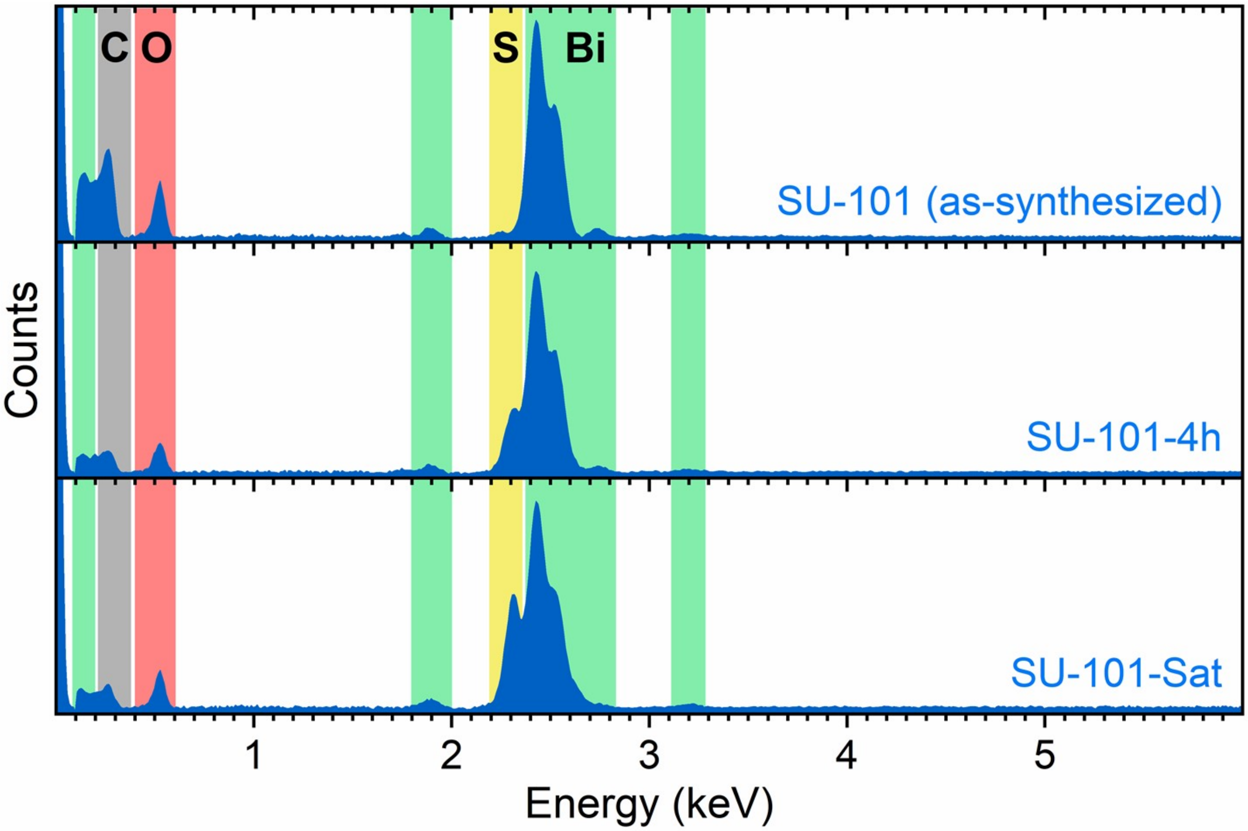

Figure S6. Elemental analysis of the SU-101 MOF samples using total-reflectance X-ray fluorescence (TXRF). Mass percentages were determined by applying an automatic baseline and selecting the detected elements with the Bruker analysis software. Note: the subtle peak at ~2.25 keV in the as-synthesized SU-101 sample does not correspond to sulfur but is a satellite bismuth peak. The sulfur peak is located at 2.3 keV (see spectra for SU-101-4h and SU-101-Sat).

Table S1: Elemental compositions of SU-101 samples from TXRF analysis.

Sample	**Mass (%)**				**Atom (%)**			
	C	**O**	**S**	**Bi**	**C**	**O**	**S**	**Bi**
SU-101 (pristine)	12.93	14.23	0	72.84	46.52	38.42	0	15.06
SU-101-4h	5.47	9.89	6.63	78.02	27.54	37.38	12.50	22.58
SU-101-Sat	5.67	11.21	11.26	71.85	25.28	37.51	18.80	18.40

Note: values represent the average from three separate measurements.

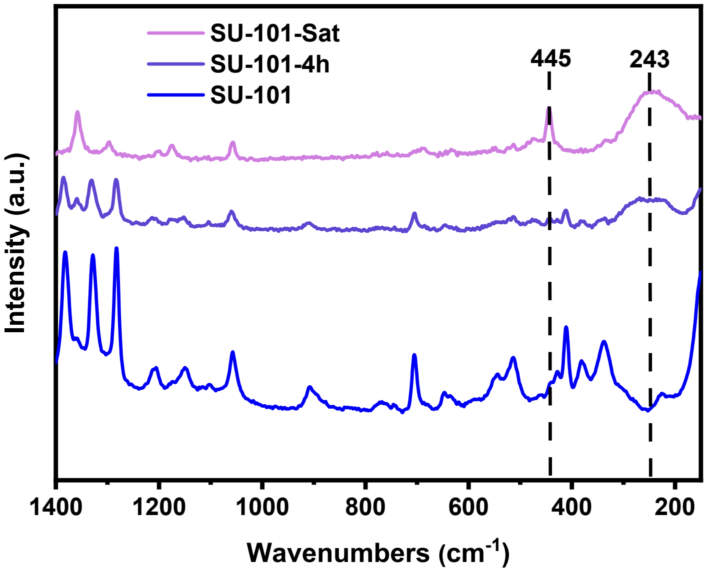

Figure S7. Raman spectra of the SU-101 MOF before and after exposure to H_2S for 4 and 12 hours.

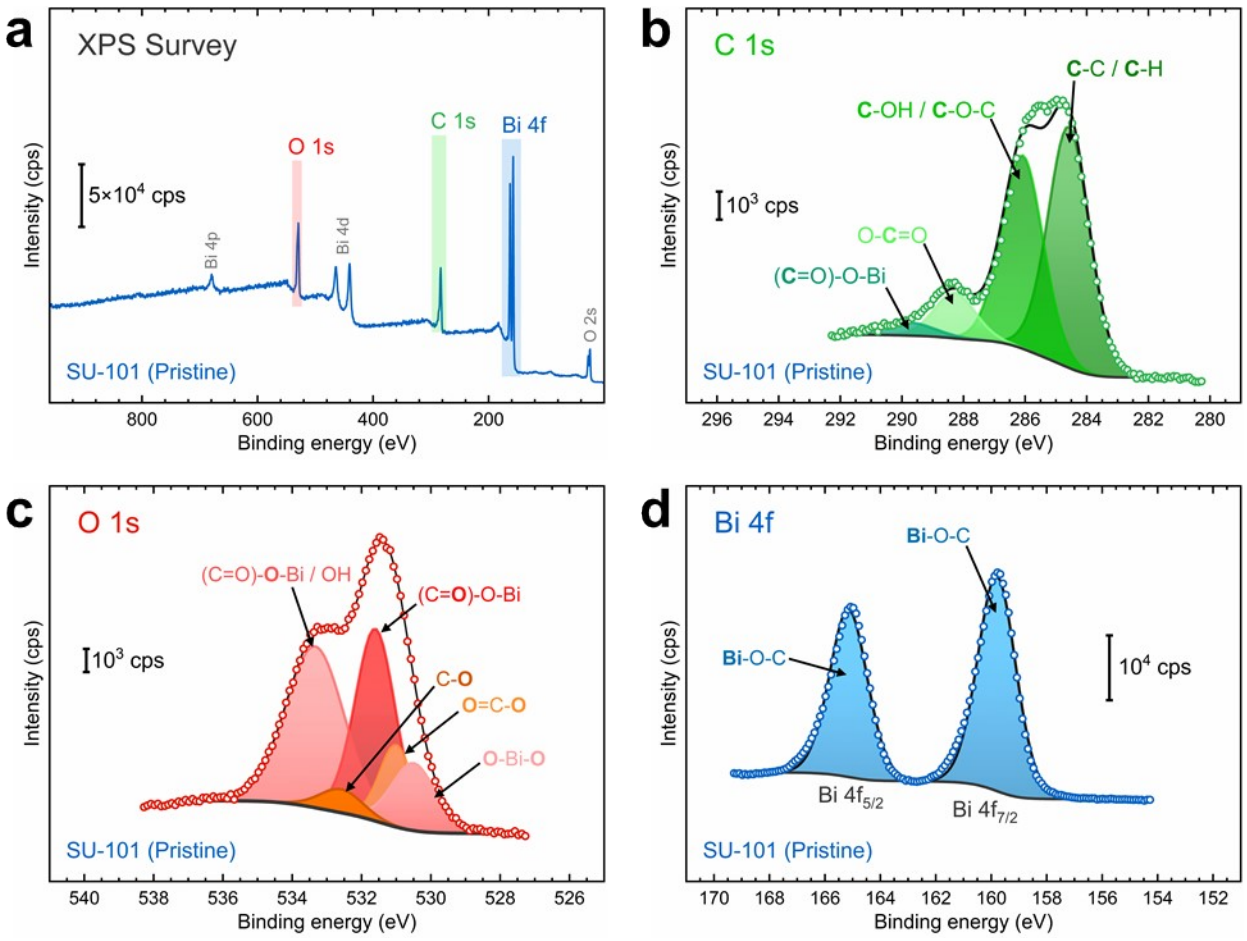

Figure S8. XPS characterization of the as-synthesized SU-101 sample: (a) XPS survey, (b) C 1s region, (c) O 1s region, and (d) Bi 4f / S 2p regions. The labels indicate the specific bonds of the functional groups related to each component fitted to the spectra. Green, red, yellow, and blue tones refer to carbon-, oxygen-, sulfur-, and bismuth-based groups.

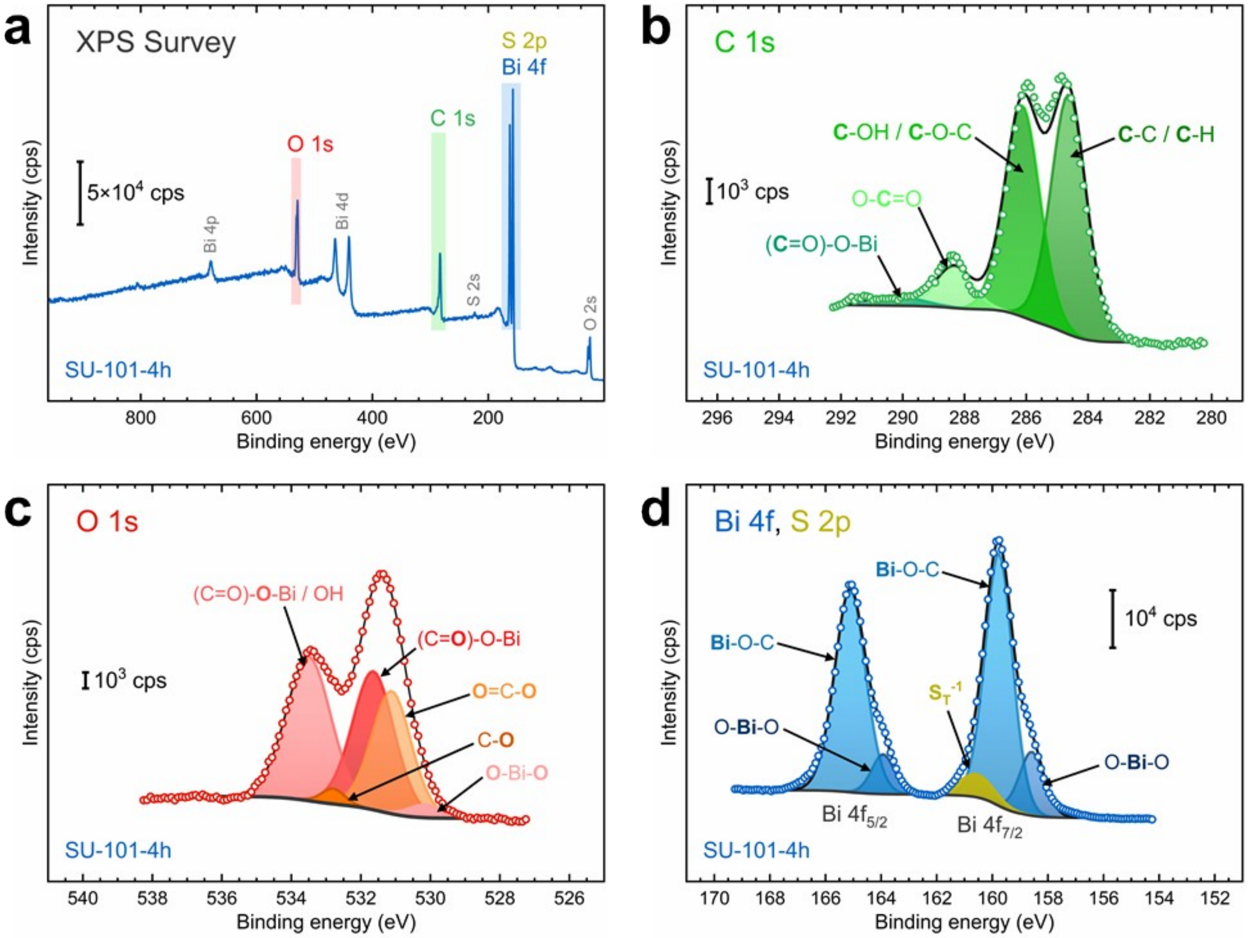

Figure S9. XPS characterization of the SU-101 sample after exposure to H_2S for 4 hours: (a) XPS survey, (b) C 1s region, (c) O 1s region, and (d) Bi 4f / S 2p regions. The labels indicate the specific bonds of the functional groups related to each component fitted to the spectra. Green, red, yellow, and blue tones refer to carbon-, oxygen-, sulfur-, and bismuth-based groups.

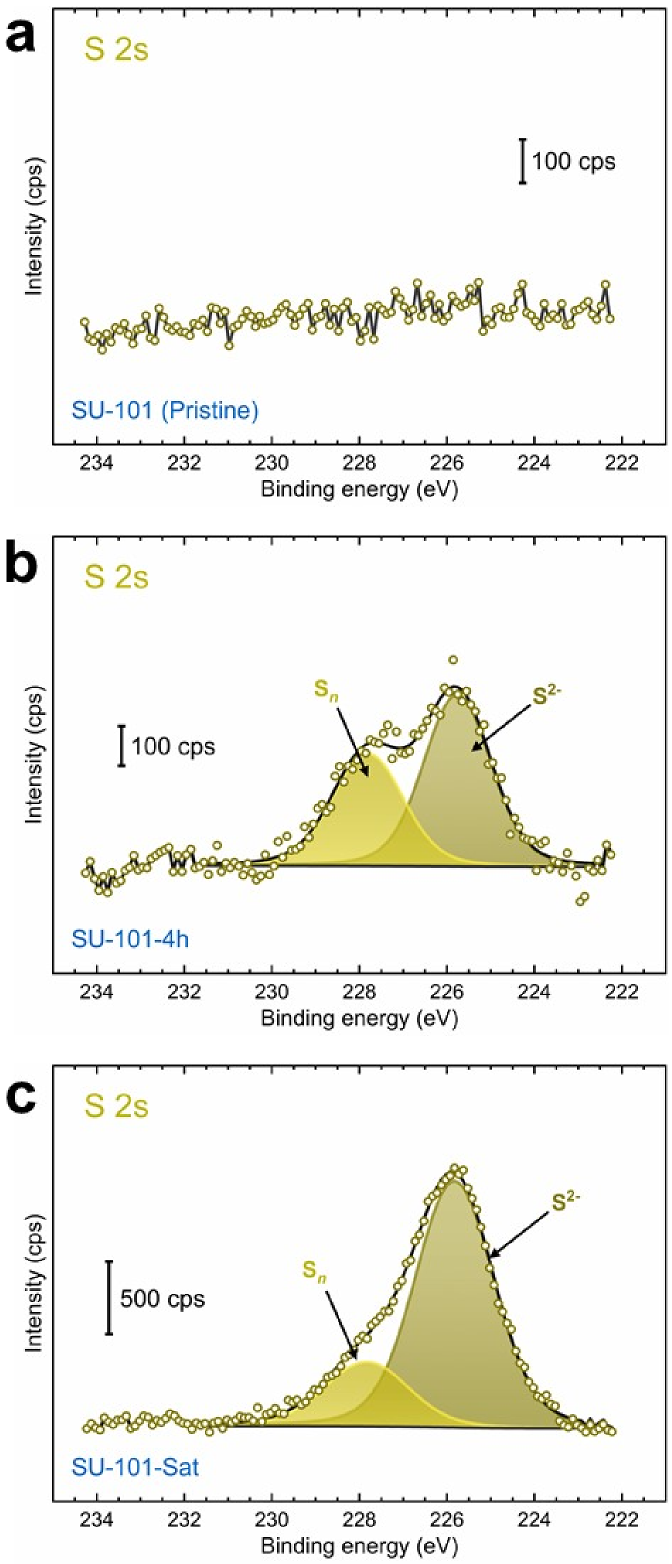

Figure S10. XPS S 2s regions for the SU-101 MOF (a) as-synthesized, (b) saturated for 4 hours, and (c) saturated overnight with H_2S. The labels indicate the specific bonds of the functional groups related to each component fitted to the spectra. Yellow tones refer to sulfur-based species.

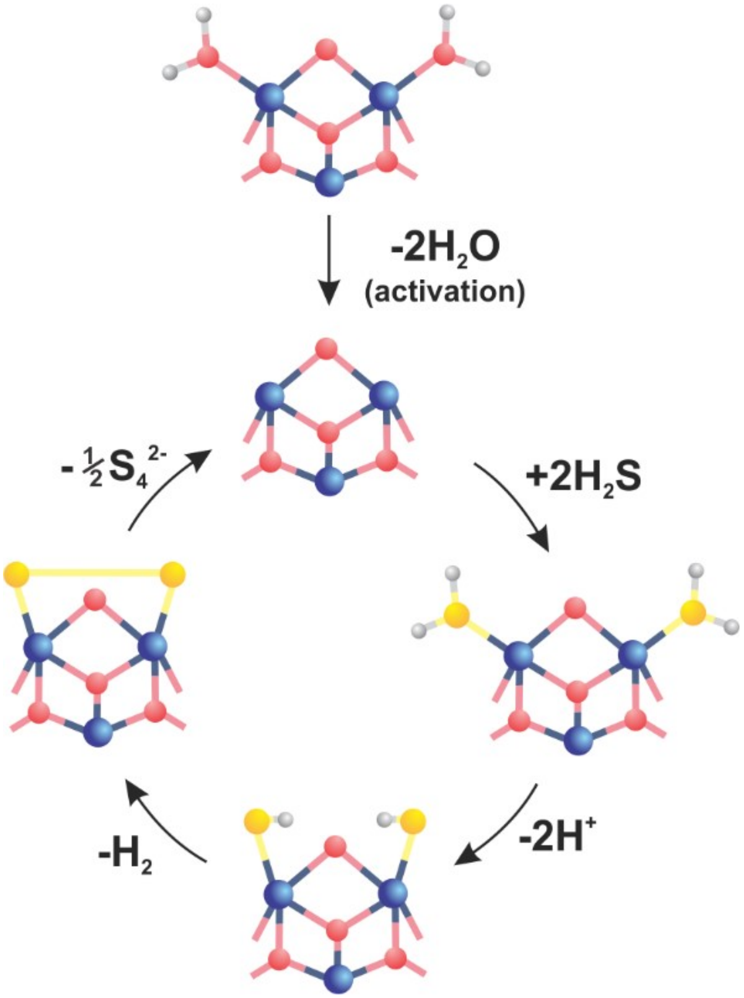

Figure S11. Proposed reaction mechanism for the formation of polysulfides mediated by the SU-101 MOF in the presence of H_2S gas. Color code for atoms: red – oxygen, blue – bismuth, yellow – sulfur, white – hydrogen.

Additional Battery Testing Results

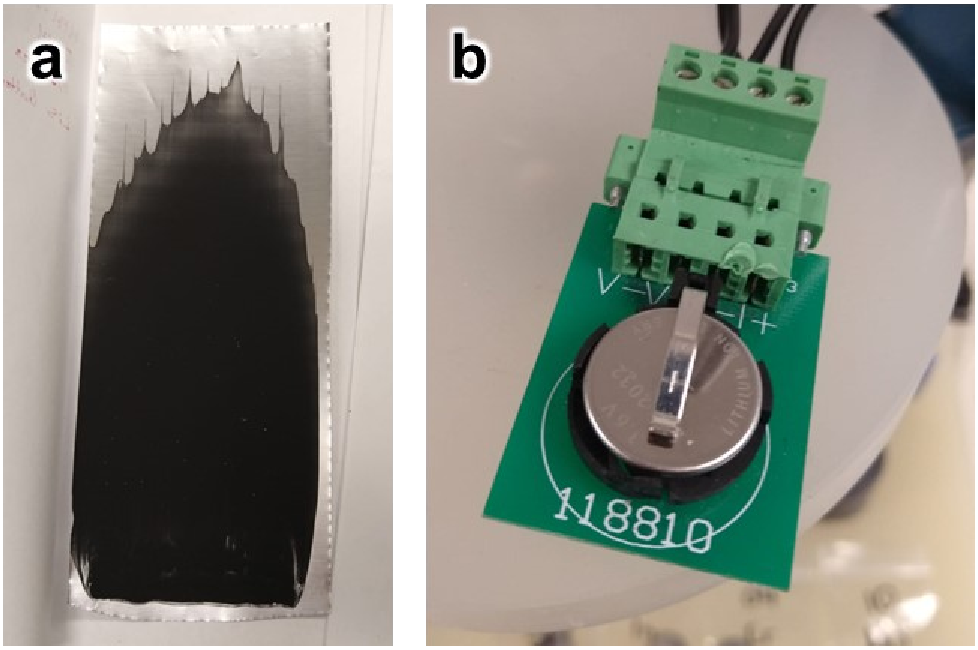

Figure S12. Preparation of MOF-containing cathodes and cell coin assembly: (a) photograph depicting the cathode slurry uniformly applied onto aluminum foil, serving as the current collector. (b) Photograph of the assembled coin cell attached to the battery holder during electrochemical measurements.

Table S2: Battery data reporting checklist.

Components and Setup			
Active material	SU-101 (active mass: 0.359 mg)		
Theoretical capacity	1672 mA·h g^{-1}		
Additive	Carbon black (Super P, TIMCAL)		
Binder	Polyvinylidene fluoride (PVDF)		
Electrolyte	DOL:DME 1:1 vol., 1 M LiTFSI + 0.2 M $LiNO_3$		
Current collector	Aluminum foil		
Separator	Celgard 2400, thickness: 25 μm		
Testing setup type	Coin cell (full cell mode)		
Anode	Li metal	*Cathode*	SU-101 MOF/Al foil
Electrode thickness	8 μm		
Electrode size	Discs with a diameter of 13 mm		

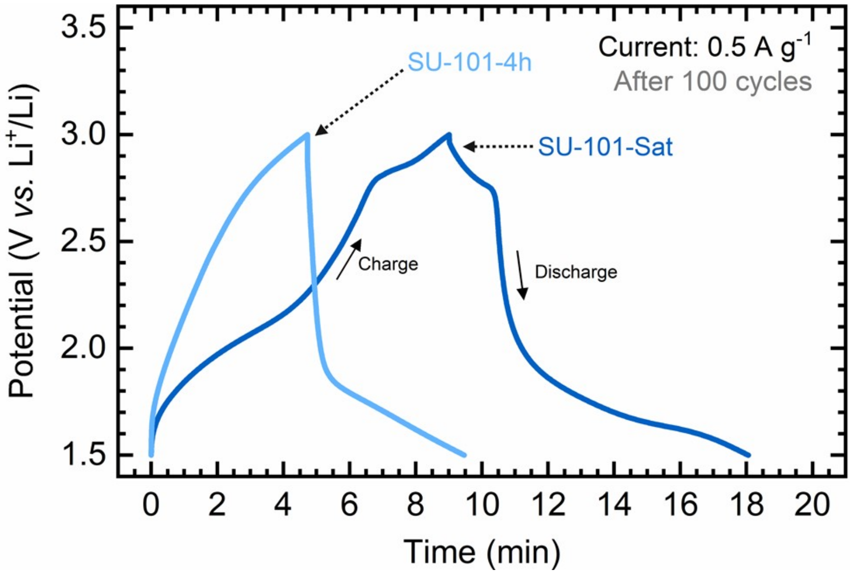

Figure S13. Galvanostatic charge-discharge curves of the SU-101 MOF cathodes after cycling at a C/2 rate (0.5 A g^{-1}) between 1.5 and 3.0 V *vs*. Li/Li$^+$. Electrolyte: 1 M LiTFSI + 0.2 M $LiNO_3$ in DME:DOL 1:1 solvent.

Supporting note: The galvanostatic charge-discharge (GCD) curve illustrates the change in cell potential as the battery is charged and discharged at a specified current (C-rate), normalized by the active mass of the cathode. In **Figure S13**, the battery is charged from 1.5 V to 3.0 V *vs*. Li/Li$^+$. Then, the battery is discharged at the same C-rate back to 1.5 V *vs*. Li/Li$^+$, completing one cycle. The apex of the curve marks the point at which the battery is fully charged before commencing discharge. The x-axis represents time, allowing for the determination of the charge and discharge durations, as well as the total cycle time. Specifically, **Figure S13** displays the charge and discharge profiles from the 100th cycle during cycling performance tests.

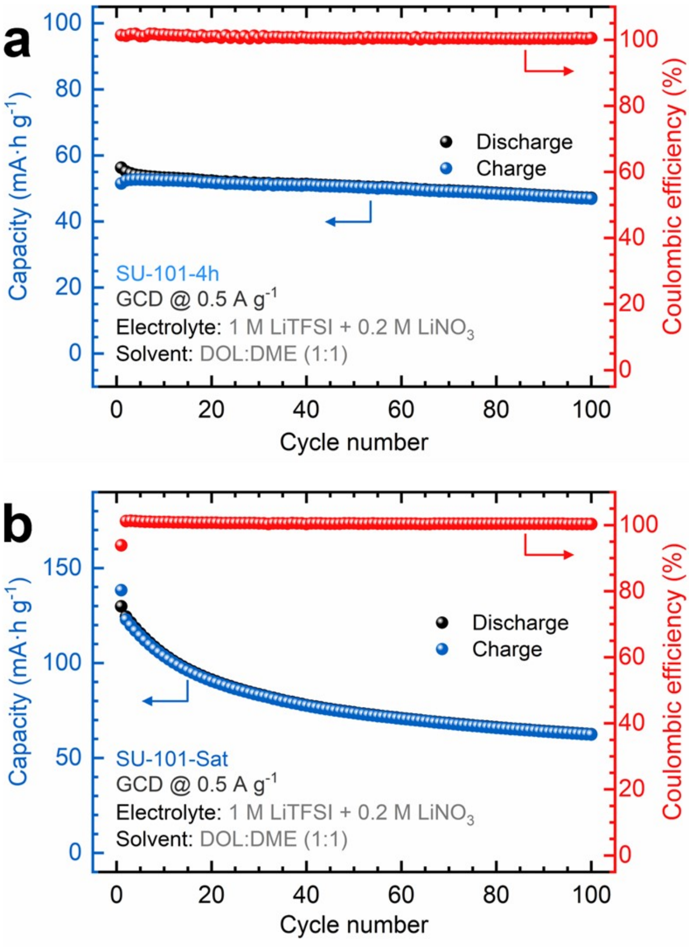

Figure S14. Cycling performance of the SU-101 MOF cathodes (a) saturated for 4h and (b) saturated overnight. The left axis indicates the capacity, while the right axis displays the coulombic efficiency. Discharge (black spheres) and charge (blue spheres) profiles are plotted concurrently. Cycling was conducted at a C/2 rate (0.5 A g^{-1}).

Supporting note: Cycling performance plots depict the capacity decay across numerous cycles. The capacity, representing the electric charge, is derived from a single GCD curve (such as **Figure S13**) by multiplying the C-rate (*i.e.,* 0.5 A g^{-1}) by the time taken to complete a charge (indicated by blue spheres) or discharge (indicated by black spheres) step. The observed decay indicates that the battery stores less charge with extended cycling, leading to quicker completion of each charge/discharge step if the C-rate remains constant. The capacity is expressed in mA·h g^{-1} following standard convention. The coulombic efficiency is calculated as the ratio of the capacities during the charge and discharge steps for each complete cycle. A coulombic efficiency of 100% indicates that the battery effectively retains and releases the same amount of electric charge during the charging and discharging processes.

Table S3: EIS analysis of different MOF cathodes before and after cycling performance tests. Parameters are derived after fitting the modified Randles equivalent circuit model.

Cathode material	OCP (V *vs.* Li/Li$^+$)	R_s (Ω)	R_{ct} (Ω)	CPE_{ct}	n	ω_{max} (Hz)	C_{dl} (μF)	Z_w
SU-101-4h (before cycling)	1.79	11.39	157.5	1.3E-5	0.77	372.9	2.16	4.1E-3
SU-101-4h (after cycling)	1.75	6.78	184.2	7.3E-6	0.85	407.5	2.28	8.9E-3
SU-101-Sat (before cycling)	1.51	6.06	72.3	1.8E-5	0.79	697.5	3.06	4.0E-3
SU-101-Sat (after cycling)	1.72	2.62	74.9	1.6E-5	0.81	614.6	3.31	7.3E-3

Supporting note: Potentiostatic EIS measurements were performed to estimate the charge transfer resistance (R_{ct}) and the double-layer capacitance (C_{dl}). EIS fitting was performed using a general Randles equivalent circuit model, including a term for the contact resistance (inset in **Figure 1b**). In this model, R_s represents the series ohmic resistance resulting from the sum of the resistance of the electrolyte, current collectors, and the resistance of the electrode material.[2–4] R_c and CPE_c denote the impedance originating from the contact between the electrode materials and the current collectors. R_{ct} and CPE_{ct} represent the total charge transfer resistance and the constant phase element characterizing the electrode-electrolyte interface, and Z_w represents the Warburg impedance. Fitted parameters were determined using the Gamry Echem Analyst software. The C_{dl} was calculated according to the following equation:[5,6]

$$C_{dl} = CPE_{ct} \times (\omega_{max})^{n-1} \qquad (1)$$

where ω_{max} (in s^{-1}) is the frequency at which the imaginary component of the Nyquist plot reaches a maximum, *n* represents the degree of depression of the semicircle compared with an ideal semicircle and has a value less than 1.0, and CPE_{ct} is the constant phase element used to model the charge-transfer process.

Table S4: EIS fitting parameters for the SU-101-Sat cathode before and after extended cycling performance tests.

SU-101-Sat	**OCP (V *vs*. Li/Li$^+$)**	**R_s (Ω)**	**R_{ct} (Ω)**	**CPE_{ct}**	**n**	**ω_{max} (Hz)**	**C_{dl} (μF)**	**Z_w**
Before	1.50	6.43	81.8	2.8E-5	0.73	692.0	2.90	1.3E-3
After	1.72	4.19	86.1	3.3E-5	0.71	628.5	3.04	2.1E-3

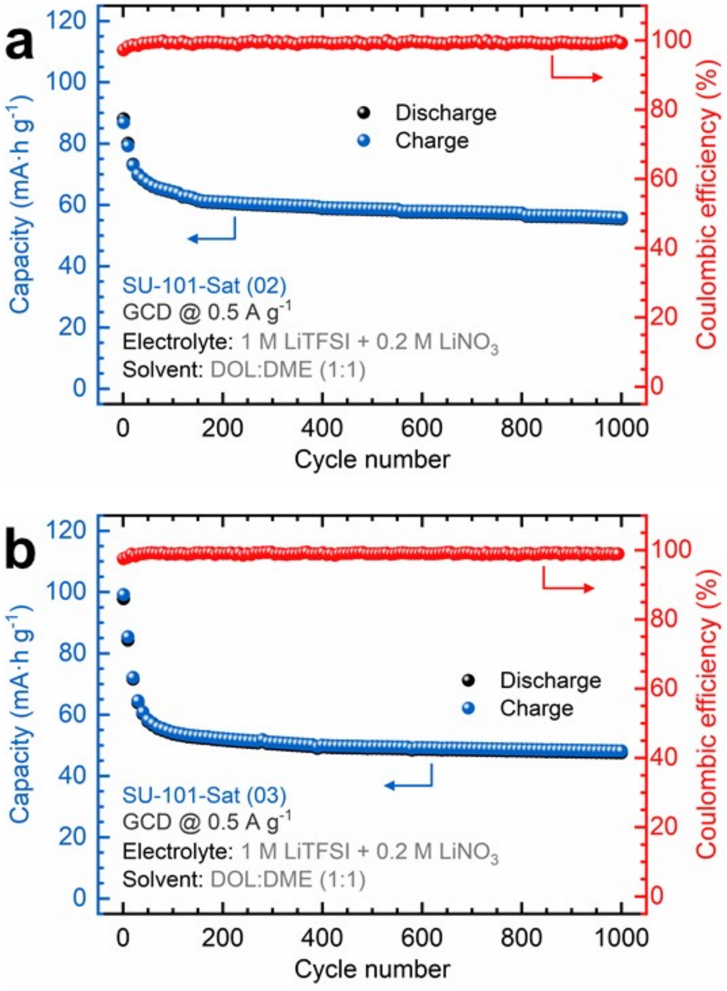

Figure S15. Additional long-term cycling tests (1000 cycles) of the SU-101-Sat MOF cathode. Coin cells with MOF cathodes, prepared in separate synthesis batches, were tested without prior electrochemical measurements before cycling. The left axis indicates the capacity, while the right axis displays the coulombic efficiency. Discharge (black spheres) and charge (blue spheres) profiles are plotted concurrently. Cycling was conducted at a C/2 rate (0.5 A g^{-1}).

Supporting note: Sample (a) exhibits an initial capacity of 88.03 mA·h g^{-1} that stabilizes at 55.44 mA·h g^{-1}. Sample (b) shows an initial capacity of 99.16 mA·h g^{-1}, stabilizing at 47.52 mA·h g^{-1}. Considering the replicate measurement shown in **Fig. 5c**, which starts at 66.60 mA·h g^{-1} and stabilizes at 33.71 mA·h g^{-1}, the SU-101-Sat cathode delivers an average initial capacity of **84.60 ± 16.55 mA·h g^{-1}** and stabilizes at an average of **45.56 ± 11.00 mA·h g^{-1}**. Thus, the average capacity retention for the SU-101-Sat cathode is approximately **53.84%**.

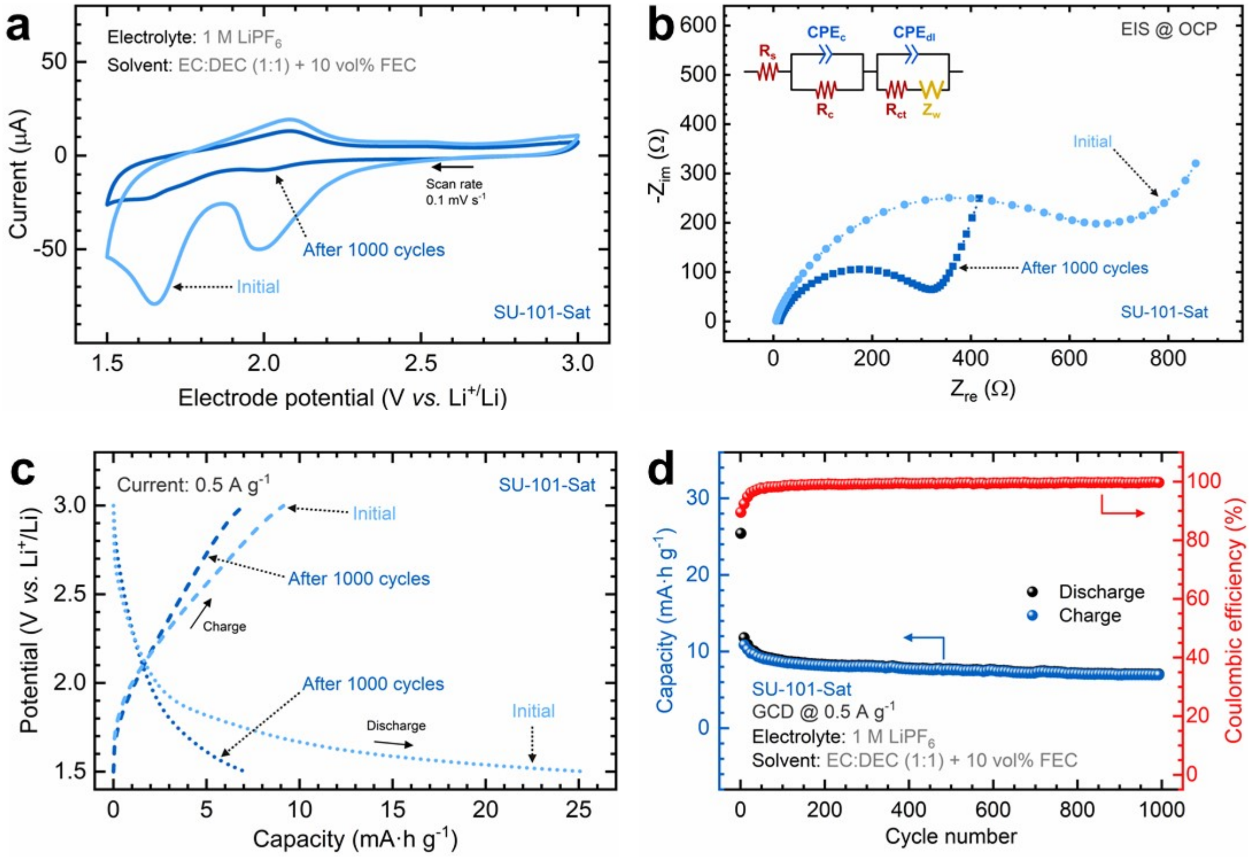

Figure S16. Battery performance tests of the SU-101-Sat MOF cathode in carbonate electrolyte: (a) Cyclic voltammograms before and after long-term cycling; the second scan is shown for each cathode, with an arrow indicating the scan direction at the specified rate. (b) Nyquist plots before and after cycling; the inset shows the equivalent circuit model used to fit the Nyquist plots. (c) Galvanostatic charge-discharge profiles before and after cycling; dashed lines represent charge profiles, dotted lines indicate discharge profiles and an arrow shows the direction of the profile. (d) Cycling performance plot displaying capacity on the left axis and coulombic efficiency on the right axis; discharge and charge profiles are plotted concurrently. Experiments were conducted at a rate of C/2 (0.5 A g^{-1}) between 1.5 and 3.0 V *vs.* Li/Li$^+$. Electrolyte: 1 M LiPF$_6$ in ethylene carbonate (EC) and diethyl carbonate (DEC) with fluoroethylene carbonate (FEC) as additive.

Table S5: EIS fitting parameters for the SU-101-Sat cathode before and after extended cycling performance tests in carbonate electrolyte.

SU-101-Sat	**OCP (V *vs.* Li/Li$^+$)**	**R$_s$ (Ω)**	**R$_{ct}$ (Ω)**	**CPE$_{ct}$**	**n**	**ω$_{max}$ (Hz)**	**C$_{dl}$ (μF)**	**Z$_w$**
Before	2.927	5.10	559.9	1.0E-5	0.87	49.7	4.70	1.1E-3
After	1.796	11.27	301.3	2.2E-5	0.76	100.6	4.51	4.1E-3

Battery Performance Metrics

Table S6: Summary of MOF-based materials employed as host for Li-S batteries.

Cathode material	Capacity (mA g h^{-1})	Current density (A g^{-1})	Cycles	Ref.
Mn-MOF	190.0	0.1	50	7
S@MOF-525(Cu)	704.0	0.5	200	8
S@Ni_3(HITP)$_2$	629.6	1.0	300	9
ZIF-67-5-S	521.0	0.5	500	10
CuBTC@S	330.0	0.2	100	11
S@Cu-TDPAT	745.0	1.0	500	12
S/MOF[Cd(L)]	799.0	0.1	50	13
MIL-101(Cr)@rGO/S	335.0	0.2	50	14
HKUST-1	240.0	0.1	50	15
NH_2-MIL-101(Al)	445.0	1.0	100	16
ZIF-8	380.0	0.1	25	17
MOF-5	540.0	0.5	50	18
ZIF-67	594.0	0.2	100	19
MIL-100(V)	500.0	0.5	200	20
Ni-MOF	611.0	0.2	100	21
SU-101-Sat	45.6	0.5	1000	This work

References

(1) Zou, Y.-H.; Wang, X.; Ning, F.; Yi, J.; Liu, Y. Implanting MWCNTs in BiCu-MOFs to Enhance Electrocatalytic CO2 Reduction to Formate. *Sep. Purif. Technol.* **2023**, *317*, 123806. https://doi.org/10.1016/j.seppur.2023.123806.

(2) Zheng, W. iR Compensation for Electrocatalysis Studies: Considerations and Recommendations. *ACS Energy Lett.* **2023**, *8*, 1952–1958. https://doi.org/10.1021/acsenergylett.3c00366.

(3) Son, Y. J.; Marquez, R. A.; Kawashima, K.; Smith, L. A.; Chukwuneke, C. E.; Babauta, J.; Mullins, C. B. Navigating iR Compensation: Practical Considerations for Accurate Study of Oxygen Evolution Catalytic Electrodes. *ACS Energy Lett.* **2023**, *8* (10), 4323–4329. https://doi.org/10.1021/acsenergylett.3c01658.

(4) Li, T.; Ma, C.; Li, Y.; Tu, F.; Jiao, C.; Li, Z.; Yao, S. In Situ Preparation of Chromium Carbide–Modified Carbon Nanofibers as Functional Electrocatalyst for Polysulfide Reduction in Lithium/Sulfur Batteries. *Ionics* **2022**, *28* (4), 1701–1711. https://doi.org/10.1007/s11581-021-04431-0.

(5) Son, Y. J.; Kawashima, K.; Wygant, B. R.; Lam, C. H.; Burrow, J. N.; Celio, H.; Dolocan, A.; Ekerdt, J. G.; Mullins, C. B. Anodized Nickel Foam for Oxygen Evolution Reaction in Fe-Free and Unpurified Alkaline Electrolytes at High Current Densities. *ACS Nano* **2021**, *15* (2), 3468–3480. https://doi.org/10.1021/acsnano.0c10788.

(6) *The Constant Phase Element - CPE*. Electrochemistry Resources. https://electrochemistryresources.com/the-constant-phase-element-cpe/ (accessed 2021-09-09).

(7) Zhang, Z.; Yoshikawa, H.; Awaga, K. Discovery of a "Bipolar Charging" Mechanism in the Solid-State Electrochemical Process of a Flexible Metal–Organic Framework. *Chem. Mater.* **2016**, *28* (5), 1298–1303. https://doi.org/10.1021/acs.chemmater.5b04075.

(8) Wang, Z.; Wang, B.; Yang, Y.; Cui, Y.; Wang, Z.; Chen, B.; Qian, G. Mixed-Metal–Organic Framework with Effective Lewis Acidic Sites for Sulfur Confinement in High-Performance Lithium–Sulfur Batteries. *ACS Appl. Mater. Interfaces* **2015**, *7* (37), 20999–21004. https://doi.org/10.1021/acsami.5b07024.

(9) Cai, D.; Lu, M.; Li, L.; Cao, J.; Chen, D.; Tu, H.; Li, J.; Han, W. A Highly Conductive MOF of Graphene Analogue Ni3(HITP)2 as a Sulfur Host for High-Performance Lithium–Sulfur Batteries. *Small* **2019**, *15* (44), 1902605. https://doi.org/10.1002/smll.201902605.

(10) Ge, X.; Li, C.; Li, Z.; Yin, L. Tannic Acid Tuned Metal-Organic Framework as a High-Efficiency Chemical Anchor of Polysulfide for Lithium-Sulfur Batteries. *Electrochimica Acta* **2018**, *281*, 700–709. https://doi.org/10.1016/j.electacta.2018.06.010.

(11) Baumann, A. E.; Aversa, G. E.; Roy, A.; Falk, M. L.; Bedford, N. M.; Thoi, V. S. Promoting Sulfur Adsorption Using Surface Cu Sites in Metal–Organic Frameworks for Lithium Sulfur Batteries. *J. Mater. Chem. A* **2018**, *6* (11), 4811–4821. https://doi.org/10.1039/C8TA01057A.

(12) Hong, X.-J.; Tan, T.-X.; Guo, Y.-K.; Tang, X.-Y.; Wang, J.-Y.; Qin, W.; Cai, Y.-P. Confinement of Polysulfides within Bi-Functional Metal–Organic Frameworks for High Performance Lithium–Sulfur Batteries. *Nanoscale* **2018**, *10* (6), 2774–2780. https://doi.org/10.1039/C7NR07118C.

(13) Li, M.-T.; Sun, Y.; Zhao, K.-S.; Wang, Z.; Wang, X.-L.; Su, Z.-M.; Xie, H.-M. Metal–Organic Framework with Aromatic Rings Tentacles: High Sulfur Storage in Li–S Batteries and Efficient Benzene Homologues Distinction. *ACS Appl. Mater. Interfaces* **2016**, *8* (48), 33183–33188. https://doi.org/10.1021/acsami.6b10946.

(14) Bao, W.; Zhang, Z.; Qu, Y.; Zhou, C.; Wang, X.; Li, J. Confine Sulfur in Mesoporous Metal–Organic Framework @ Reduced Graphene Oxide for Lithium Sulfur Battery. *Journal of Alloys and Compounds* **2014**, *582*, 334–340. https://doi.org/10.1016/j.jallcom.2013.08.056.

(15) Zhang, Z.; An, Y.; Feng, J.; Ci, L.; Duan, B.; Huang, W.; Dong, C.; Xiong, S. Carbon Coated Copper Sulfides Nanosheets Synthesized via Directly Sulfurizing Metal-Organic Frameworks for Lithium Batteries. *Materials Letters* **2016**, *181*, 340–344. https://doi.org/10.1016/j.matlet.2016.06.066.

(16) Zhang, H.; Zhao, Z.; Hou, Y.-N.; Tang, Y.; Dong, Y.; Wang, S.; Hu, X.; Zhang, Z.; Wang, X.; Qiu, J. Nanopore-Confined g-C_3N_4 Nanodots in N, S Co-Doped Hollow Porous Carbon with Boosted Capacity for Lithium–Sulfur Batteries. *J. Mater. Chem. A* **2018**, *6* (16), 7133–7141. https://doi.org/10.1039/C8TA00529J.

(17) Fu, Y.; Li, Y.; Zhou, R.; Zhang, Y.; Chen, S.; Song, Y.; Wang, L. Co3O4 nanoparticles@MOF-5-Derived Porous Carbon Composites as Anode Materials with Superior Lithium Storage Performance. *Journal of Alloys and Compounds* **2018**, *749*, 645–651. https://doi.org/10.1016/j.jallcom.2018.03.338.

(18) Bao, W.; Zhang, Z.; Zhou, C.; Lai, Y.; Li, J. Multi-Walled Carbon Nanotubes @ Mesoporous Carbon Hybrid Nanocomposites from Carbonized Multi-Walled Carbon Nanotubes @ Metal–Organic Framework for Lithium Sulfur Battery. *Journal of Power Sources* **2014**, *248*, 570–576. https://doi.org/10.1016/j.jpowsour.2013.09.132.

(19) Xiao, D.; Li, Q.; Zhang, H.; Ma, Y.; Lu, C.; Chen, C.; Liu, Y.; Yuan, S. A Sulfur Host Based on Cobalt–Graphitic Carbon Nanocages for High Performance Lithium–Sulfur Batteries. *J. Mater. Chem. A* **2017**, *5* (47), 24901–24908. https://doi.org/10.1039/C7TA08483H.

(20) Hou, Y.; Mao, H.; Xu, L. MIL-100(V) and MIL-100(V)/rGO with Various Valence States of Vanadium Ions as Sulfur Cathode Hosts for Lithium-Sulfur Batteries. *Nano Res.* **2017**, *10* (1), 344–353. https://doi.org/10.1007/s12274-016-1326-0.

(21) Zheng, J.; Tian, J.; Wu, D.; Gu, M.; Xu, W.; Wang, C.; Gao, F.; Engelhard, M. H.; Zhang, J.-G.; Liu, J.; Xiao, J. Lewis Acid–Base Interactions between Polysulfides and Metal Organic Framework in Lithium Sulfur Batteries. *Nano Lett.* **2014**, *14* (5), 2345–2352. https://doi.org/10.1021/nl404721h.